IUST
Iran University of Science and Technology

Iranian Journal of Electrical and Electronic Engineering

Journal Homepage: ijeee.iust.ac.ir

Design and Simulation of Synchronous Reluctance Motor in IE4 Efficiency Class

Mohammad Abshari*, and Mansour Rafiee * (C.A.)

Abstract: The present study aims to design, analyze, and simulate the synchronous reluctance motor (SynRM) based on the IEC90L frame and IE4 efficiency class. Initially, the permissible losses are calculated for the SynRM considering the given efficiency class. The SynRM is then designed using the calculated losses to generate the highest possible output power. In order to achieve optimal performance in terms of output power and power factor (PF), a parametric per-unit system is utilized for SynRM analysis, and the dimensions of various parts of the motor are determined based on design inputs (copper losses and magnetic loading). Subsequently, given this parametric model and the changing range of per-unit parameters, the characteristics of the available motors are thoroughly monitored with respect to output parameters, and the motor model is selected. To validate the analytical model, the finite element analysis (FEA) is conducted for the selected model, and the simulation results are compared with those of the analysis method and design inputs. Ultimately, to enhance overall motor performance, an optimization process was conducted, followed by a comprehensive evaluation of the optimized model to assess efficiency and torque improvements.

Keywords: AC Motor, Synchronous Reluctance Motor (SynRM), High Efficiency Calss

1 Introduction

THE increasing energy cost and a boost in environmental pollution have driven technology to detect ways of manufacturing products with lower energy consumption. Electric motors have gained tremendous attention due to consuming more than half of the electrical energy generated in the world and being utilized in various industries 0. Therefore, using motors with higher efficiency is of paramount importance to reduce energy consumption and the emission of polluting gases such as CO_2.

One of the effective measures taken to lessen energy consumption is the establishment of new standards and regulations on motor efficiency, which forces manufacturers and designers to augment the efficiency of their products0. For instance, the definition of the Ultra-premium/IE5 efficiency class has been modified in the second edition of the IEC 60034-30 standard, the mandatory IE3 efficiency class in North America and some countries since 2015, and the IE4 efficiency class for motors with a power range of 75 to 200 kW has also been mandatory since July 2023 in the European Union.

Synchronous reluctance motors (SynRMs) are one of the most promising options for meeting efficiency requirements owing to their high efficiency, low cost, and the absence of permanent magnets (PMs) on their rotors [3]-[7]. Compared to conventional induction motors (IMs), the SynRMs possess higher levels of efficiency class due to operating at synchronous speed and eliminating rotor induction losses 0. In general, 25% of losses in IMs are rotor ohmic losses [9]. Elimination of ohmic losses in SynRMs, they would have cooler rotors in comparison with IMs. Other advantages of these motors over conventional IMs include their robustness, lower manufacturing costs, and the absence of conductors on the rotor, which facilitates their easier maintenance. Despite the aforementioned advantage points, these motors, as compared to IMs, suffer from a

Iranian Journal of Electrical & Electronic Engineering, 2026.
Paper first received 16 Mar 2025 and accepted 27 Jul 2025.
* The authors are with the Faculty of Electrical Engineering, Shahid Beheshti University, Tehran, Iran
E-mail: m_abshari@sbu.ac.ir, m_rafiee @sbu.ac.ir
Corresponding Author: Mansour Rafiee

number of disadvantages, including lack of line-start capability, torque ripple, lower power factor (PF), and more complicated controllability, all of which have led to the slowdown in the industrial use of SynRMs[10]. In recent years, numerous efforts have been made to overcome the inherent challenges of these motors. In order to improve the performance of SynRMs, PMs, as PM assistance elevating the PF and torque, are incorporated into their structure [11]-[13]. The insertion of PMs in the rotor empowers SynRMs to operate at PF similar to those of other PM motors [14]. Another challenge is their design complexity compared to the other motors. Due to the specific geometry and numerous parameters of the rotor and the high sensitivity of torque and torque ripple to these parameters, it is difficult to devise a standard design method for these motors. However, in recent years artificial intelligence methods have been employed for the design and optimization of these motors, better performance in terms of torque and ripple [15]-[18].Despite the above-mentioned issues, the policy of reducing energy consumption and the necessity of utilizing electric motors with higher efficiency classes have led to a boost in the production and supply of this type of motor in the electric motor market over the past few years. Accordingly, major manufacturers have introduced these motors with a wide range (0.55-350 kW) of power to the market [19]-[20].

In this study, a SynRM is designed based on the IEC frame used for constructing IMs in the same power (output power) class. To this end, the initial design inputs are determined considering the IEC standard efficiency classes. The final model is then selected using parametric modeling in such a way that this model has the highest power output for a fixed amount of loss. Eventually, the finite element analysis is carried out based on the initial design parameters and the selected model.

2 Design Equations

The motor losses are calculated considering the IE4 efficiency class. Based on this efficiency class, the minimum efficiency of a 1.1 kW motor is 87% [21]. Therefore, the minimum loss regardless of mechanical and rotational losses for this power class is 150 watts 0. The dimensions of the active areas of R and L are determined by the IEC90L standard frame. Other initial design parameters are listed in Table (1). The thermal loading of the motor is dependent on the amount of copper losses, and the type of cooling is influenced by the stator peripheral surface, as expressed in (1) [22].

$$k_{cool} = \frac{P_{cu}}{2\pi RL} = \frac{3}{2}.\frac{R_s i_{rated}^2}{2\pi RL} \quad (1)$$

where R_s denotes the stator resistance and i_{rated} signifies the thermal rated current. In this equation, R and L are the stator outer radius and the stator length, respectively. The values of k_{cool} are 1.5 - 3 kW/m^3 for natural ventilation, 5 - 12 kW/m^3 for fan ventilation, and 12 - 20 kW/m^3 for the water-cooling system [22].

Table 1. Parameters of design inputs.

Parameter	Value	Units
Output power	1.1	kW
Speed (ω_m)	1500	rpm
Peak of iron flux density (B_{Fe})	1.4	T
Efficiency	≥ 87%	-
Pole pairs (p)	2	-
Number of slots per pole per phase (q)	3	-
Airgap length (g)	0.3	mm
Stack length (IEC-90L)	75	mm
Stator outer radius (IEC-90L)	67	mm
Shaft diameter	24	mm
Slot filling factor (k_{fill})	0.4	-
Input voltage	400	volt
Number of rotor flux barriers ($n_{barrier}$)	3	-
Copper temperature	80	°C

After selecting the values of initial copper losses and k_{cool} and the computation of the stator resistance with respect to the dimensional parameters of the motor, the thermal rated current is determined by using (2).

$$i_{rated} = \sqrt{k_{cool}.\frac{N_s^2}{9}.\frac{L}{L+L_{end}}.\frac{k_{fill}}{\rho}.\pi R A_{slots}} \quad (2)$$

where N_s signifies the number of winding turns per phase, k_{fill} is the slot filling factor, ρ represents the specific copper resistivity, and A_{slots} is the total area allocated to the stator slots. The end-winding length is denoted by L_{end}, which is calculated through (3) for the distributed winding.

$$L_{end} = 2l_t + (r + \frac{l_t}{2})\frac{\pi}{p} \quad (3)$$

In this equation, p signifies the number of pole pairs, and l_t is the stator tooth length. In order to evaluate the motor outputs in terms of design inputs and the motor geometric parameters (Fig. 1), two per-unit parameters are defined according to (4) and (5) [23].

$$x = \frac{r}{R} \quad (4)$$

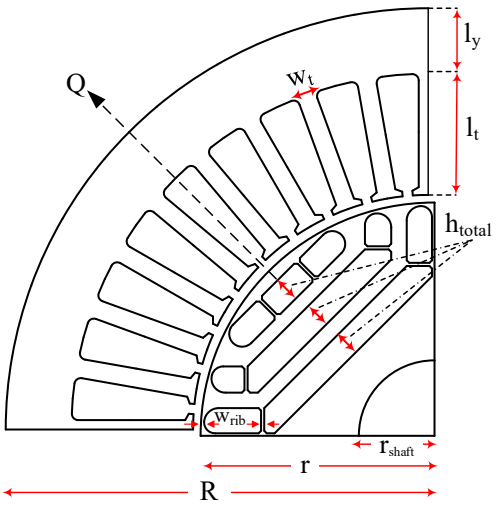

Fig 1. Motor geometric parameters.

$$b = \frac{B_g}{B_{FE}} \tag{5}$$

In which r symbolizes the rotor radius and R is the stator outer radius. The peak flux density in the airgap and the stator iron (tooth or yoke) are denoted by B_g and B_{FE}, respectively.

2.1 Design of d-Axis

Axis d in SynRMs possesses the highest permeance. The iron core in the stator and rotor is thus designed based on the d-axis equations. Assuming that the sinusoidal flux density (the fundamental component) in the airgap has a peak value of B_g and there is no magnetic saturation, the d-axis flux under the one pole in the airgap is expressed as:

$$\varphi_d = \frac{2rLB_g}{p} \tag{6}$$

By inserting (4) and (5) into (6), equation (7) is obtained.

$$\phi_d = \frac{2rLB_{Fe}}{p} xb \tag{7}$$

The thickness of the yoke (l_y) is also calculated using (8), and the tooth width is achieved with respect to flux density in the airgap through (9).

$$l_y = \frac{\pi}{2}\frac{R}{p} bx \tag{8}$$

$$w_t = \frac{2\pi R}{6qp} bx \tag{9}$$

In (9), q is the number of slots per pole per phase. Given the ideal magnetic material, the d-axis current required for creating flux density in the airgap is computed through (10).

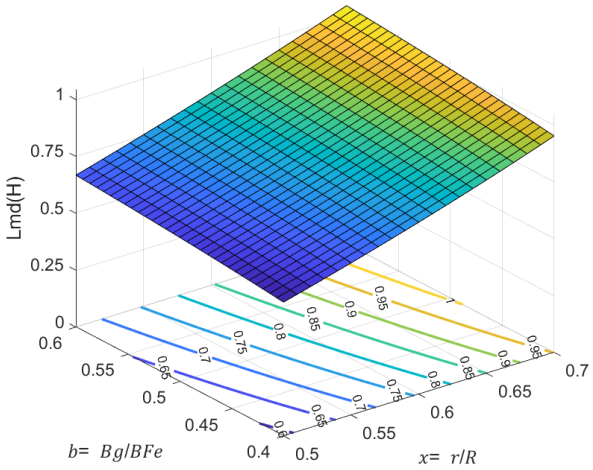

Fig 2. Magnetizing inductance of d-axis in permissible ranges of x and b geometric parameters.

$$i_d = \frac{\pi}{3}\frac{k_c g}{\mu}\frac{p}{k_w N_s} B_{FE}.b \tag{10}$$

where K_c and K_w signify Carter's coefficient and the winding factor, respectively [24]. This current establishes flux linkage with respect to iron flux density, which can be calculated from (11).

$$\lambda_{md} = 2RL\frac{k_w N_s}{p} B_{FE}.xb \tag{11}$$

The value of λ_{md} depends on both per-unit parameters x and b. The magnetizing inductance of this axis, L_{md}, is also achieved from the ratio of the flux linkage to the d-axis current. Variations in L_{md} values for the permissible ranges of x and b parameters are depicted in Fig. 2. The L_{md} value is raised with an increase in the values of b and x.

2.2 Design of q-Axis

The parameters of the q-axis are primarily specified based on rotor geometry and the design of flux barriers on this axis. The magnetizing inductance of this axis, L_{mq}, comprises two main components: the circulating term (L_{cq}) and the flow-through term (L_{fq})[25]. In the first component (L_{cq}), the flux lines cross the air gap but are circulating in the tips of the rotor flux guides. However, in the second component (L_{fq}), the flux lines cross all the flux barriers along the q-axis. The per-unit value of the circulating term based on L_{md} is computed through (12).

$$\frac{L_{cq}}{L_{md}} = 1 - \frac{4}{\pi}\sum_{k=1}^{n_{barrier}} f_k^2 \alpha_k \tag{12}$$

In this equation, $n_{barrier}$ is the number of flux barriers, f_k is the stator Magneto-Motor Force (MMF) of the kth

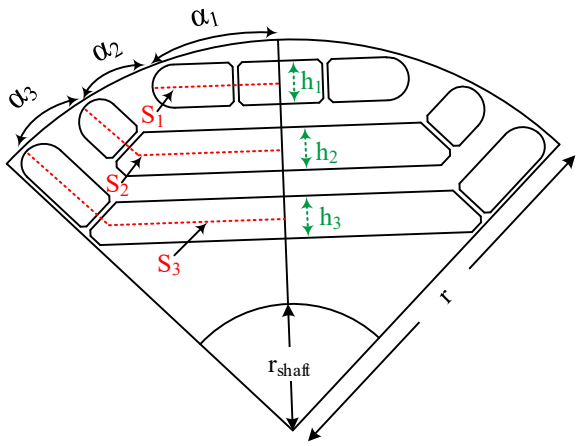

Fig 3. Parameters of rotor geometry.

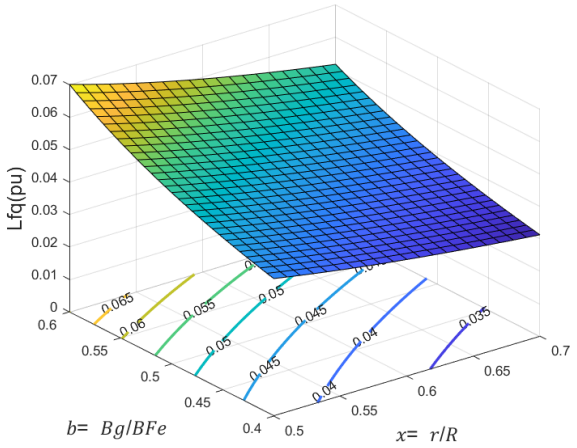

Fig 4. Per-unit values of L_{fq} based on L_{md}.

flux barrier, and α_k is kth flux barrier position along the airgap. Fig. 3 illustrates different parameters of rotor geometry required for calculating these two flux terms. The value of L_{cq} is dependent on the number of flux barriers. With an increase in the number of flux barriers, the value of the inductance is reduced. When the number of flux barriers is more than three in each rotor pole, this value is less than 3% [26]. Equation (12) indicates that the thickness of flux barriers (h_k) has no significant impact on this value. The angle of flux barriers is determined in such a way as to minimize torque ripples [27]. The selected values of parameters α_1, α_2, and α_3 are 17, 11.5, and 11.5 degrees, respectively.

The other component is the flow-through term (L_{fq}), which is a major part of the q-axis inductance. The per-unit value of this component is calculated using (13).

$$\frac{L_{fq}}{L_{md}} = 1 - \frac{4}{\pi}\frac{\mathrm{P}k_c g}{Rx}\sum_{k=1}^{n_{barrier}} f_k^2 \frac{s_k}{h_{c,k}} \tag{13}$$

where S_k is the length of the flux barriers along the d-axis, and h_c signifies the thickness of the flux barriers along the q-axis. The thickness of the flux barriers exerts a substantial influence on this inductance component. An increase in the thickness of the flux barriers raises the value of L_{fq}. Excessive escalations in the thickness of the flux barriers reduce the overall thickness of the rotor iron, leading to saturation and an increase in magnetizing current. In order to prevent saturation, the overall thickness of rotor flux guides should be at least equal to the thickness of the stator yoke. In this way, the overall thickness of the rotor flux barriers is limited. As a result, considering Fig. 1, equation (14) can be expressed as follows:

$$h_{total} = r - r_{shaft} - l_y \tag{14}$$

The thickness of each flux barrier is also estimated using (15).

$$h_1 = h_2 = h_3 = \frac{h_{total}}{3} \tag{15}$$

Fig. 4 indicates variations of L_{fq} for the given values of rotor geometry.

2.3 Effect of Ribs

Ribs are mechanical connections that are magnetically short-circuited and provide a very low reluctance flux path. The low thickness of ribs in the rotor as well as their saturation restrict the flux linkage path. Nevertheless, in order to make a more accurate calculation of L_{mq} and decline output torque induced by the magnetic effects of these mechanical connections should be considered in the modeling. The flux passing through these connections is computed using the (16).

$$\phi_{rib} = 2B_{ribs}S_{ribs}L \tag{16}$$

B_{ribs} is flux density in ribs which corresponds to rotor saturated iron. This value for the iron used in this modeling (M310-50A) equals 1.8 Tesla. The flux linkage value of the ribs is calculated through (17).

$$\lambda_{rib} = \frac{4}{\pi}k_w N_s W_{rib(total)} L B_{rib} \tag{17}$$

where $W_{rib(total)}$ signifies the thickness of all ribs in the flux barriers. The thicknesses of ribs at the end of the flux barriers and of ribs inside the flux barriers were considered to 0.4 mm and 0.5 mm, respectively. Although these connections are not proportional to q-axis current I_q, their impact on the torque and PF can be assessed by inserting one of the components of the q-axis inductance, called L_{rq}, in the model. Fig. 5 depicts variations of this parameter (L_{rq}) for different values of x and b values.

2.4 Leakage Inductance

Leakage inductance affects the PF. Therefore, it is essential to consider this parameter in the design of the SynRM to achieve a precise estimation of its PF.

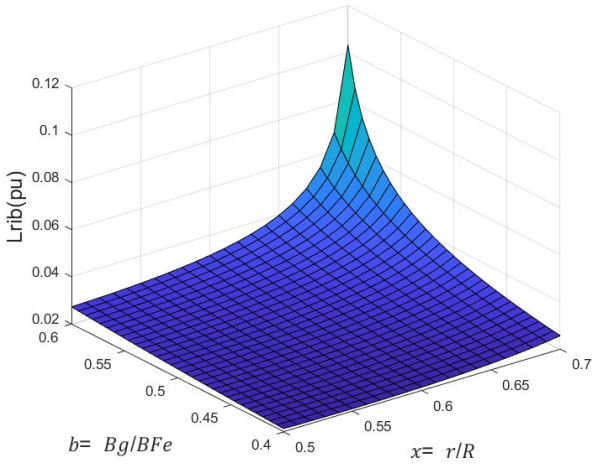

Fig 5. Per-unit values of L_{rq} based on L_{md}.

The leakage inductance can be measured through (18) [28].

$$L_{\sigma} = \frac{2\mu_0 N_S^2 L}{pq} p_s \tag{18}$$

where P_s denotes the permeance of the stator slot, this value, determined by the geometry of the stator slot, is acquired by (19) [10].

$$p_s = \frac{d_0}{c_0} + \frac{d_1}{c_0} \frac{\ln(\frac{c_1}{c_0})}{\frac{c_1}{c_0} - 1} + \frac{d_2}{c_2} \frac{\beta^2 - \frac{\beta^4}{4} - \ln(\beta) - \frac{3}{4}}{(1-\beta)(1-\beta^2)^2} \tag{19}$$

In this equation, β is equal to c_1/c_2. The geometric parameters of the stator slots required for the computation of the permeance are presented in Fig. 6. In Fig. 7, the per-unit values of leakage inductance are provided based on the d-axis magnetizing inductance. The leakage inductance is augmented by a rise in magnetic loading.

3 Output Equations

The output power of the SynRM is obtained using the following:

$$P_{out} = T_e \omega_m = \frac{3}{2} p \omega_m (\lambda_{ds} i_{qs} - \lambda_{qs} i_{ds}) \tag{20}$$

where ω_m is the motor speed. The flux linkages along the d-axis and q-axis are symbolized as λ_d and λ_q, respectively. These values are estimated from (21).

$$\begin{aligned} \lambda_{ds} &= L_{ls} i_{ds} + L_{md} i_{ds} = L_{ds} i_{ds} \\ \lambda_{qs} &= L_{ls} i_{qs} + L_{mq} i_{qs} = L_{qs} i_{qs} \end{aligned} \tag{21}$$

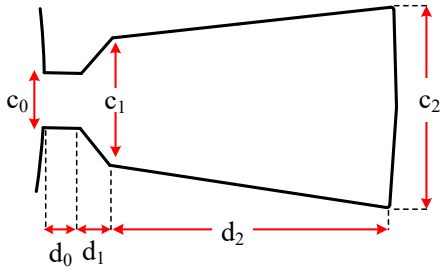

Fig 6. Geometric parameters of stator slots.

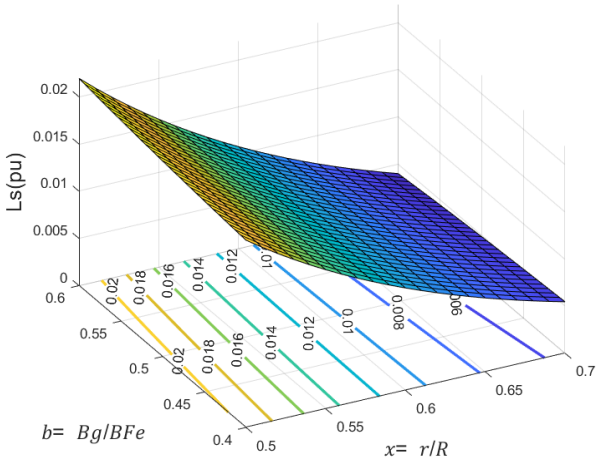

Fig 7. Per-unit values of leakage inductance based on L_{md}.

In equation (21), L_{ls}, L_{md}, and L_{mq} signify the leakage inductance, d-axis magnetizing inductance, and q-axis magnetizing inductance, respectively. By inserting (21) into (20), the output power of the SynRM is achieved as follows:

$$\begin{aligned} p_{out} &= \frac{3}{2} p \omega_m (L_{md} - L_{mq}) i_d i_q = \\ &\frac{3}{2} p \omega_m (1 - \frac{L_{md}}{L_{mq}}) L_{md} i_d i_q = \frac{3}{2} p \omega_m k_{dq} \lambda_{md} i_q \end{aligned} \tag{22}$$

As equation (22) indicates, the output power is directly associated with λ_{md} and i_q. In this equation, k_{dq} is the magnetic anisotropy factor of the rotor, which is defined as:

$$k_{dq} = (1 - \frac{L_{md}}{L_{mq}}) \tag{23}$$

This factor (k_{dq}) is highly dependent on the parameters of rotor geometry and the rotor flux barriers. The closer the rotor magnetic design is to the ideal rotor, the closer the k_{dq} value is to one. Given (11), when the parameters of x and b are boosted, the value of λ_{md} is raised, resulting in the in these two parameters brings about a reduction in the total area of slots in the motor.

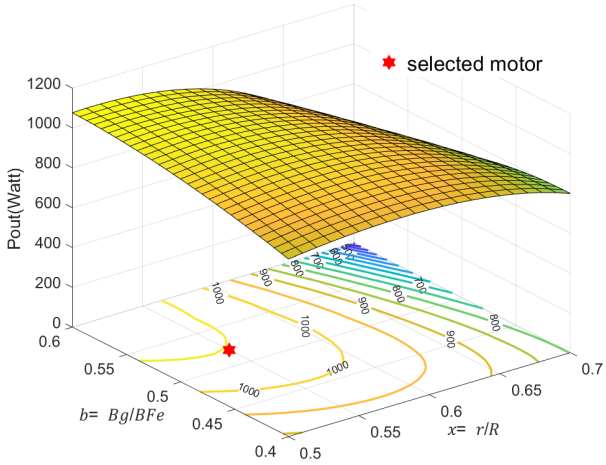

Fig 8. Parametric design plane obtained with the analytical model: output power is functions of x and b.

Based on (2), the nominal and q-axis currents are consequently declined ($i_q \le \sqrt{i_{rated}^2 - i_d^2}$). Therefore, to maximize output power, it is required to keep a tradeoff between λ_{md} (magnetic loading) and currents (electrical loading). Considering this issue, the output power of the motor for all the permissible values of x and b is depicted in Fig. 8. The lines drawn on the bx plane are the constant output power contours.

The PF of the motor is also regarded as a crucial performance parameter in SynRMs. Irrespective of the stator resistance, the PF can be written as:

$$\cos\varphi = \sin(\gamma - \delta) \tag{24}$$

where δ and γ denote the angles of the flux linkage and the current with respect to the d-axis, respectively. The maximum possible value of the PF in this motor can be measured by equation (25) [29].

$$PF_{\max} = \frac{L_d - L_q}{L_d + L_q} = \frac{L_{md} - L_{mq}}{L_{md} + L_{mq} - 2L_\sigma} = \frac{k_{dq}}{2 - k_{dq} - \frac{L_\sigma}{L_{md}}} \tag{25}$$

The first influential element in the PF is the k_{dq} coefficient, which reflects the magnetic characteristics of the rotor. With small values of k_{dq}, the PF is low even if the leakage inductance is zero. Another effective parameter is the leakage inductance, which, based on (18) and (19), is concerning the dimensions and shape of the stator slots. Fig. 9 illustrates variations in the PF of the SynRM for the feasible values of parameters x and b. The lines drawn on the bx plane show the constant PF contours. The stator slot opening value in the calculations and graphs is 25% of the slot pitch.

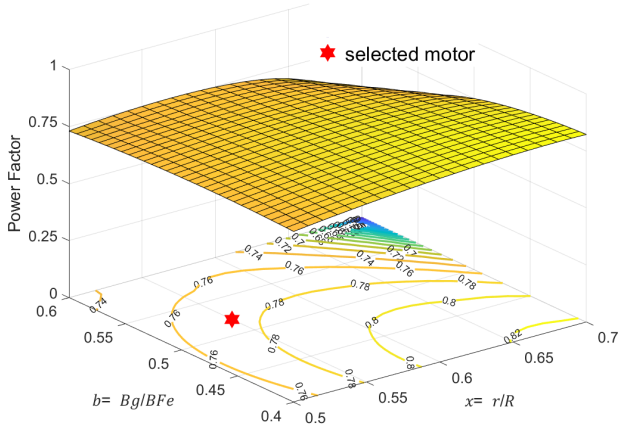

Fig 9. Parametric design plane obtained with the analytical model: power factor is functions of x and b.

3.1 Selection of Motor

The constant contours of the output power and PF drawn on the bx plane (Fig.s 8 and 9) indicate that by changing the values of parameters b and x, it is not feasible to simultaneously achieve maximum values for both output power and PF in the SynRM. To select the final motor model for finite element analysis, it is required to make a tradeoff between the output power and PF. The red star point marked in Fig.s 8 and 9, in which parameters x and b equal 0.55 and 0.52, respectively, were selected as the candidate model finite element analysis validation. Based on these chosen values, the output torque and PF are equal to 6.8 N.m and 0.77, respectively. Other parameters and specifications of the motor based on these two selected parameters (b and x) are presented in Table 2.

4 Evaluation of Selected Motor by Finite Element

The motor simulation was performed with the finite element software at the rated current of the motor using the parameters provided in Table 2. Fig. 10 exhibits the magnetic flux density in various parts of the rotor and stator. The flux density amplitude in different parts of the motor strongly confirms the selected values for the final design model. Fig. 11 illustrates the distribution of flux density and its fundamental harmonic in the airgap. The graphs presented in this figure exhibit a strong correlation with the selected values for selected motor. Fig.12 illustrates the motor's torque output under Maximum Torque per Ampere (MTPA) strategy, as determined at both the rated current and 1.5 times the rated current. The finite element analysis (FEA) results indicate that the obtained torque values are lower than those predicted by the analytical model. This discrepancy may stem from not considering saturation in modeling process and the non-optimal selection of the overall thickness of flux barriers. Furthermore, under

rated operating conditions, the torque ripple exceeds 30%. Although the simulation results for selected motor are consistent with the computational model, torque profiles in this figure suggest that further optimization-particularly of the torque ripple-is necessary to enhance overall performance.

Table 2. Parameters of selected motor

Parameter	Value	Units
Number of turns in series per phase (N_s)	450	-
Peak of rated current (i_{rated})	3.5	Amp
Current density	4.4	Amp/mm^2
Stator resistance (R_s)	6.3	Ω
Yoke thickness (l_y)	10.5	mm
Tooth width (W_t)	3.2	mm
Tooth length (l_t)	18	mm
Area of one slot	103	mm^2
Overall thickness of flux barriers (h_{total})	12	mm
q-Axis inductance (L_q)	93	mH
d-Axis inductance (L_d)	920	mH
Leakage inductance (L_σ)	18	mH

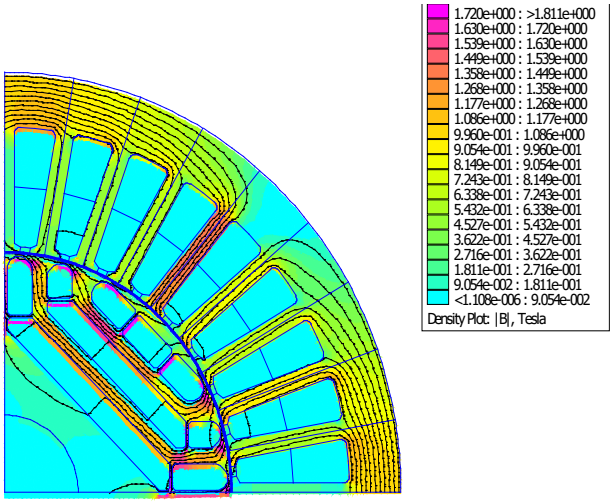

Fig 10. Magnetic flux density in selected motor.

Considering the constant copper in motor design computations, to assess the selected motor in the intended efficiency class, the core losses were calculated in the rated conditions with the finite element software based on the loss characteristics of iron used. Fig. 13 indicates the core losses and their types in different parts of the selected motor. The total loss is computed to be 15.6 watts. The sum of this value and the copper losses considered during the initial modeling phase is lower than the total allowable losses prescribed for this efficiency class.

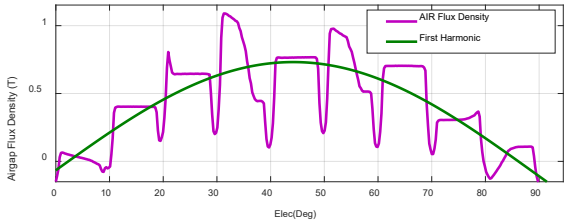

Fig 11. Airgap flux density distribution under one pole (B_g) for selected motor.

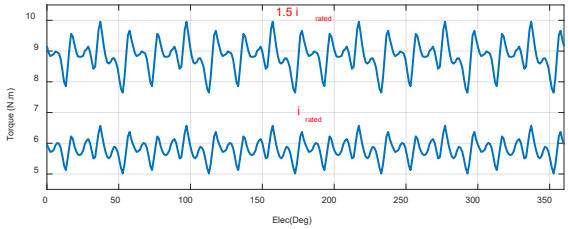

Fig 12. Torque-position waveforms calculated with the respective MTPA current phase angles.

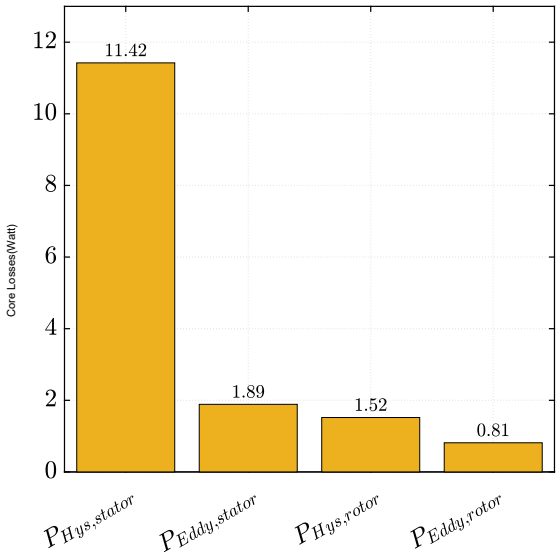

Fig 13. Core losses of selected motor at rated conditions based on specifications of iron used in the design (M310-50A).

5 Performance Optimization

Multi-objective differential evolution (MODE) optimization algorithm, integrated with magnetostatic finite element, is employed to enhance performance SynRM. MODE algorithm exhibits exceptional performance in the optimization of electrical machines, particularly in achieving rapid convergence and ensuring high repeatability of results[30]. The two optimization objectives are the maximization of the torque and

minimizing the torque ripple. During the optimization process, motor performance is assessed at a constant current equal to the thermal rated current, as defined in equation (2). This approach reflects practical design limitations and ensures thermal feasibility. By maximizing the torque at this current level, the algorithm effectively enhances the output power-to-copper loss ratio, which is directly linked to the motor's overall efficiency.

Table 3. Limits of the search space for optimization

Parameter	max	min	Units
α_1	13	21	Deg
α_2	7.5	15	Deg
α_3	7.5	15	Deg
h_1	3	5	mm
h_2	3	5	mm
h_3	3	5	mm
γ	30	80	Deg

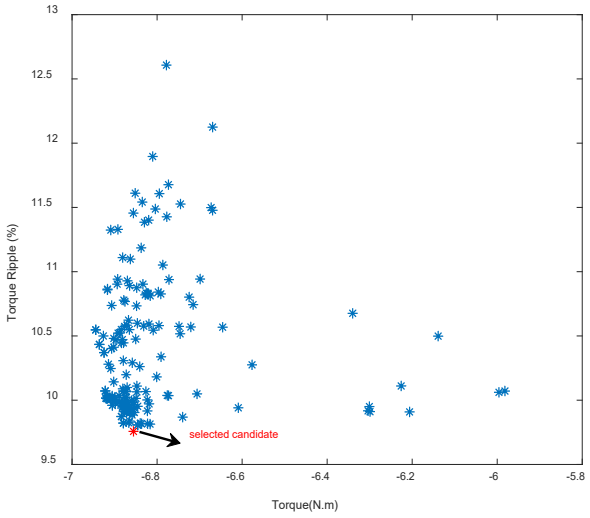

Fig 14. Pareto front for average torque and torque ripple for 2400 calls.

To ensure the manufacturability of the rotors in the optimization process, a minimum radial steel thickness of 1.5 mm is considered between adjacent barriers, thereby limiting the maximum space available for the barriers. Throughout the optimization process, the thicknesses of both the central and tangential ribs were considered as fixed parameters. For each motor, a single current vector, expressed in *dq* coordinates, was simulated. The resulting output torque was then evaluated at five distinct rotor positions distributed across one stator slot pitch [31].

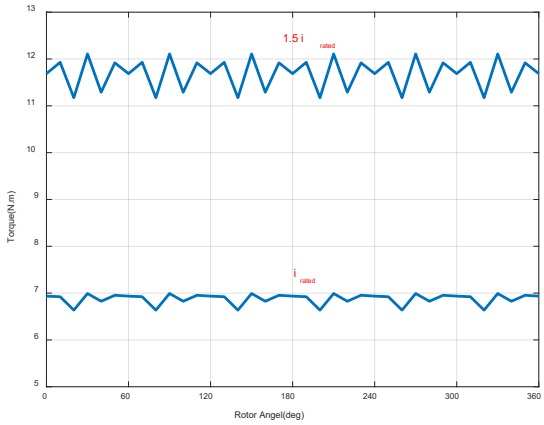

Fig 15. Torque-position waveforms calculated with the respective MTPA current phase angles.

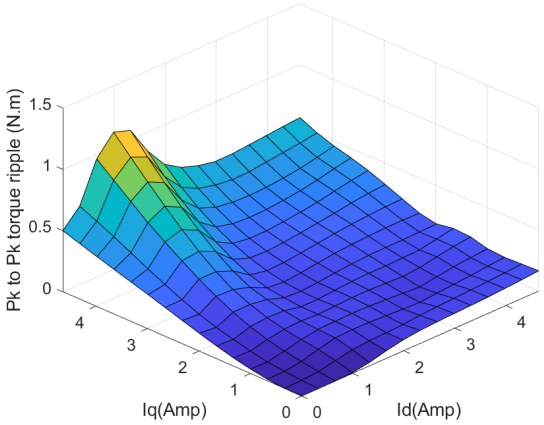

Fig 16. Torque ripple surface over the i_d, i_q plane, according to FEA.

Last but not least, γ, the phase angle current in the *dq* frame, is a key factor in achieving MTPA condition, denoted as γ_{MTPA}. Since γ_{MTPA} is highly dependent on motor geometry, it cannot be determined analytically for each new candidate and typically requires multiple finite element simulations to identify accurately. To reduce computational time, γ is treated as an additional design variable in the optimization process. Each motor candidate is evaluated at a single γ value, randomly selected by the optimization algorithm. As the algorithm seeks to maximize average torque, it naturally converges towards configurations where the chosen γ closely approximates γ_{MTPA}, thus achieving MTPA implicitly without requiring multiple simulations[18].

The set of search bounds used in the paper is reported in Table 3. The results Pareto front after 2400 motors (60 individuals are iterated over 40 generations) reported in Figs. 14. To achieve Pareto fronts with a great density of solutions, a penalty function was incorporated despite the limited population size. Specifically, candidate motors exhibiting a torque ripple exceeding 15% or an

average torque below 5 Nm were penalized, as these values significantly deviated from the performance specifications. Consequently, the final Pareto front is concentrated within the region of interest in the torque–torque ripple design space. The results of the optimization demonstrate a 15% enhancement in torque, accompanied by a reduction in torque ripple to below 10%. This is confirmed by Fig15, which illustrates the torque waveforms at various current levels.

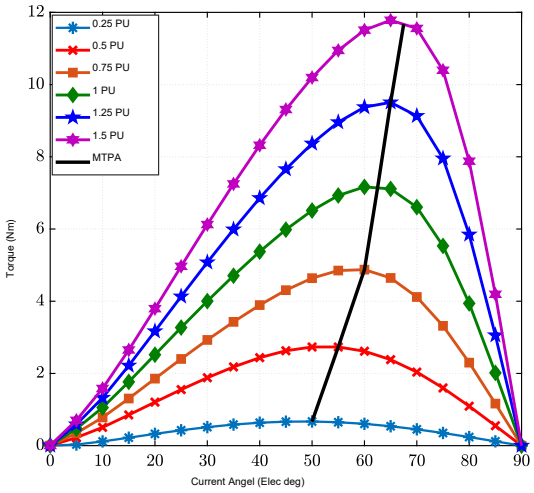

Fig 17. Torque Vs current angle (γ) diagram at different currents.

A comparative assessment of Fig.15 indicates that the observed reduction in torque ripple is notably significant across both simulated current levels. Additionally, to more comprehensive evaluation of the motor's torque ripple across various operating points, Fig.16 presents a 3D surface plot depicting torque ripple as a function of i_d and i_q components, extending up to 1.5 times the rated current. This profile provides influence of current vector variations on torque ripple magnitude, thereby aiding in the refinement of motor control strategies.

5.1 Optimal Model Evaluation

MTPA is a fundamental performance metric in electric motor design, representing the operating condition in which maximum torque is produced for a given current, thereby optimizing efficiency. Fig. 17 presents the torque versus current angle (γ) graphs for currents at levels ranging from 0.25 to 1.5 times the rated value. The black curve is corresponding to the MTPA strategy in the motor. The graphs drawn in this Fig.17 clearly demonstrates that the optimal current phase angle for achieving maximum torque is not fixed and it varies as a function of the current amplitude. The range of variation for this angle, across the current levels considered in the simulation, is approximately 15 degrees. This variation indicates that, under different loading conditions, the alignment of the current vector respect to the d-axis must be dynamically adjusted to sustain optimal torque production. Fig.18 presents the PF of the optimized motor as a function of different current levels. The depicted curves reveal that the maximum PF is achieved at a current phase angle of approximately 70°. In contrast, the condition for maximum torque occurs at a current phase angle that is lower than 70°. This observation clearly indicates that the optimal condition for torque production does not coincide with the optimal PF. Consequently, this divergence highlights an inherent trade-off in the design and operation of the motor, where MTPA and optimal PF require distinct current phase angle settings.

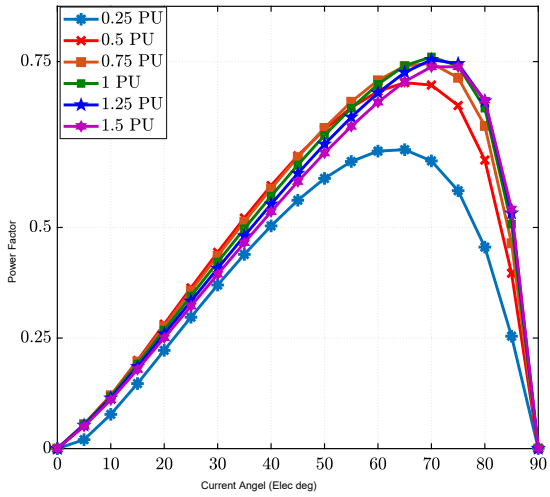

Fig 18. Power factor Vs current angle (γ) diagram at different currents.

The torque-efficiency map provides a critical tool for evaluating performance of motors. Its detailed depiction of efficiency as a function of both speed and torque not only clarifies the operational characteristics of the motor but also provides a strong framework for subsequent design refinements aimed at enhancing overall energy conversion efficiency. Fig. 19 illustrates efficiency map of optimized motor, highlighting the relationship between torque and rotor speed within the specified operational boundary. The graph indicates a progressive improvement in efficiency as the speed approaches 1500 rpm from lower values, suggesting that losses such as copper, and iron losses are minimized at or near the rated speed. At the rated speed of 1500 rpm, the optimized motor operates near its optimal performance point. Efficiency and torque values in this region reveal that the motor attains high efficiency levels, with the contour lines or data points clustered around maximum efficiency near rated torque outputs. This operating condition arises from a deliberate design strategy in which the electromagnetic parameters are chosen to ensure that the motor operates within its optimal performance envelope within the operating range of

1500 rpm. Fig. 20 provides a detailed comparison of core and copper losses between the optimized motor and a similar motor in the IE4 efficiency class. A comparative analysis of these two graphs indicates that the proposed motor exhibits an overall reduction of 9% in total losses relative to same power motor within the IE4 efficiency class. These improvements not only enhance efficiency under nominal operating conditions but also contribute to improved reliability and extended motor lifespan. Moreover, this effective loss minimization reduces energy consumption and environmental impact, aligning with contemporary sustainability objectives in industrial applications. Overall, the loss distribution diagram substantiates the efficacy of the design optimizations applied, thereby confirming the motor's superior performance relative to IE4 class.

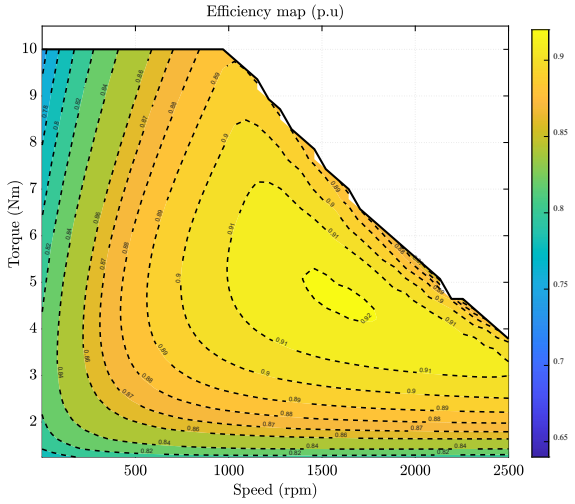

Fig 19. Efficiency map of optimized motor under MTPA conditions.

6 Conclusion

In the present study, a 1.1 kW and 1500 rpm SynRM was designed, and simulated. In the design method, an analytical model was utilized to determine the highest output power based on a constant loss. Through this analytical method, the output characteristics of the existing motors were extracted, and the model was selected based on the output performance parameters of the motor. The finite element simulation was conducted for the selected model. The results of the finite element simulation verify the accuracy and precision of the design method in terms of magnetic loading in various parts of the motor. In order to evaluate the design process with regard to the considered efficiency class, the core losses of the motor were computed at nominal conditions for selected motor.

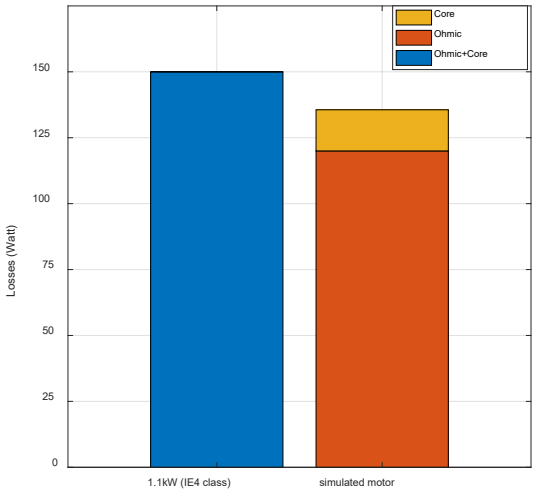

Fig 20. Comparison of losses in designed motor with losses in motors of IE4 efficiency class (irrespective of mechanical losses).

Ultimately, A multi-objective optimization was performed on the selected motor. Evaluations of torque and efficiency across various operating points confirmed that the optimization effectively tuned on the selected motor to perform optimally around its rated speed and torque. The results of the simulation in terms of motor outputs and losses substantiated the accuracy and precision of the motor design process.

References

[1] International Energy Agency, World Energy Outlook IEA, PP. 284-309 , Paris 2013. [Online]. available: https://www.iea.org/reports/world-energy-outlook-2016.

[2] A. T. De Almeida, F. J. T. E. Ferreira, A. Q. Duarte, "Technical and Economical Considerations on Super High-Efficiency Three-Phase Motors," *IEEE Transactions on Industry Applications*, Vol. 50, No. 3, pp. 2103–2114, May/Jun. 2014.

[3] T. He, Y. Wang, M. Bao, J. Li, S. Feng, R. Qu , "Design and Validation of a High-Efficiency Synchronous Reluctance Motor," I*EEE Transactions on Industry Applications(Early Access),* Feb. 2025.

[4] S. Ferrari, R. Paolo, D. Gaetano, G. Pellegrino, "Flux and loss map based evaluation of the efficiency map of synchronous machines," *IEEE Transactions on Industry Applications*, vol. 59, No. 2, pp. 1500-1509, 2022.

[5] S. Stipetic, D. Zarko, and N. Cavar, "Design Methodology for Series of IE4/IE5 Synchronous Reluctance Motors Based on Radial Scaling," *XIII*

International Conference on Electrical Machines (ICEM), Alexandroupoli, Greece, Sep. 2018.

[6] V. Dmitrievskii, V. Prakht, and V. Kazakbaev, "IE5 Energy-efficiency Class Synchronous Reluctance Motor with Fractional Slot Winding," *IEEE Transactions on Industry Applications*, vol. 55, No. 5, pp.4676–4684, Sep. 2019.

[7] M. S. Lim, J. P. y. Hong, "Design of High Efficiency Wound Field Synchronous Machine With Winding Connection ChangeMethod," *IEEE Transactions on Energy Conversion,* Vol.33, No. 4, pp.1978–1987, 2018.

[8] I. Boldea, T. Lucian, *Reluctance electric machines design and control*. CRC Press, 2018.

[9] H. Mahmoud, M. Degano, G. Bacco, N. Bianchi, C. Gerada, "Synchronous reluctance motor iron losses: Analytical model and optimization," *IEEE Energy Conversion Congress and Exposition (ECCE)*, pp. 1640-1647, 2018.

[10] M. Murataliyev, M. Degano, M. Di Nardo, N. Bianchi, C. Gerada, "Synchronous reluctance machines: A comprehensive review and technology comparison," *Proceedings of the IEEE*, Vol. 110, No. 3, pp. 382-399, 2022.

[11] A. M. Ajamloo, A. Ghaheri, M. N. Ibrahim and P. Sergeant, "Principle of Torque-Axis Alignment in New Asymmetric PM Synchronous Reluctance Machines: Towards Less-Rare-Earth PM Machines," *IEEE Transactions on Transportation Electrification(Early Access),* Sep. 2024.

[12] M. Al-ani, A. Walker, G. Vakil, D. Gerada, C. Gerada, and K. Paciura, "Modifications to PM-assisted Synchronous Reluctance Machine to Achieve Rare-Earth Free Heavy-duty Traction," *IEEE Journal of Emerging and Selected Topics in Power Electronics*, Vol. 11, No. 2, pp. 2029-2038, 2022.

[13] A. M. Ajamloo, A. Ghaheri, M. N. Ibrahim and P. Sergeant, "Investigation of Different Pole Configurations in New Asymmetric Permanent Magnet Synchronous Reluctance Machines, " *IEEE Transactions on Magnetics(Early Access),* Jan. 2025.

[14] M.Akçomak, Z. P. Sibel, "Design of a 2.2 kW 4-Pole IE5 Efficiency Class Line-Start Permanent Magnet Synchronous Motor. " *2024 6th Global Power, Energy and Communication Conference (GPECOM),* pp. 190-198, NoV. 2024.

[15] M. Murataliyev, M. Degano, M. Di Nardo, N. Bianchi, A. Tessarolo, W. Jara, M. Galea, and C. Gerada, "Homothetic design in synchronous reluctance machines and effects on torque ripple," *IEEE Transactions on Energy Conversion*, Vol. 36, No. 3, pp.2195-2205, 2020.

[16] F. Cupertino, G. Pellegrino, and C. Gerada,"Design of synchronous reluctance motors with multiobjective optimization algorithms," *IEEE Transactions on Industry Applications*, Vol. 50, No. 6, pp. 3617–3627,Nov. 2014.

[17] N. Bianchi, M. Degano, and E. Fornasiero, "Sensitivity analysis of torque ripple reduction of synchronous reluctance and interior PM motors," *Transactions on Industry Applications*, vol. 51, no. 1, pp. 187–195, Jan. 2015.

[18] G. Pellegrino, T. M. Jahns, N. Bianchi, W. L. Soong, and F. Cupertino, *The Rediscovery of Synchronous Reluctance and Ferrite Permanent Magnet Motors*. Tutorial Course Notes, Cham, Switzerland: Springer, 2016.

[19] ABB SynRM Motors Without Rare Earth Magnets Deliver Ultra-Premium Energy Efficiency. 2022, [Online].Available: https://magneticsmag.com/abb-synrm-motorswithout-rare-earth-magnets-deliver-ultrapremium-energy-efficiency/.

[20] REEL SuPremE Motor: Premium IE5/IE4 Efficiency Without Magnets. Accessed: Dec. 26, 2023. [Online]. Available: https://www.ksb.com/REELen/productssolutions/Synchronous_reluctance_motors/reelsupreme-ie5/.

[21] Ed. 2, Committee Draft for Vote, 2/1687/CDV: Rotating Electrical Machines—Part 2-1: *Standard Method for Determining Losses and Efficiency from Tests (Excluding Machines for Traction Vehicles)*, IEC Std. 60034-2-1, Jan. 2013.

[22] T. A. Lipo, T. J. E. Miller, A. Vagati, I. Boldea, L. Malesani, T. Fukao, "*Synchronous reluctance drives tutorial*," presented at the IEEE Industry Applications Society Annual Meeting, Denver, CO, USA, Oct. 1994.

[23] Ferrari, S., Pellegrino, G., "Feafix: Fea refinement of design equations for synchronous reluctance machines." *IEEE Transactions on Industry Applications*, Vol. 56, no. 1, pp. 256-266, 2019.

[24] H. A. Toliyat, , B. G. Kliman, *Handbook of electric motors*. Vol. 120. CRC press, 2018.

[25] A.Vagati, G. Franceschini, I. Marongiu, G. P. Troglia, "Design criteria of high performance synchronous reluctance motors," *Conference record of the 1992 IEEE industry applications society annual meeting.*, vol. 1, pp. 66–73, Oct. 1992.

[26] G. Pellegrino, P. Guglielmi, A. Vagati and F. Villata, “Core Losses and Torque Ripple in IPM Machines: Dedicated Modeling and Design Tradeoff,” *IEEE Transactions on Industry Applications*, Vol. 46, No. 6, pp. 2381-2391, Nov.-Dec. 2010.

[27] A. Vagati, A. Fratta, G. Franceschini, P. Rosso, “ AC motors for high-performance drives: a design-based comparison,” *IEEE Transactions on Industry Applications*, Vol. 32, No. 5, pp. 1211-9. Sep 1996.

[28] T. A. Lipo, *Introduction to AC machine design*. John Wiley & Sons, 2017.

[29] D. A. Staton, T. J. E. Miller, and S. E.Wood, “ Maximizing the saliency ratio of the synchronous reluctance motor,” *IEE Proceedings B (Electric Power Applications)*. Vol. 140, No. 4. IET, 1993.

[30] M. Cheng, X. Zhao, M. Dhimish, W. Qiu and S. Niu, “A Review of Data-Driven Surrogate Models for Design Optimization of Electric Motors,” in *IEEE Transactions on Transportation Electrification*, Vol. 10, no. 4, pp. 8413-8431, Dec. 2024.

[31] D. Mingardi and N. Bianchi, "Line-Start PM-Assisted Synchronous Motor Design, Optimization, and Tests," in *IEEE Transactions on Industrial Electronics*, vol. 64, no. 12, pp. 9739-9747, Dec. 2017.

Biographies

Mohammad abshari received the M.Sc in electrical machines and drive from Isfahan University of Technology (IUT), Isfahan, Iran, 2011. He is currently pursuing the Ph.D. degree in electrical engineering in Shahid Beheshti University (SBU). His research interests include electrical machine design and multiphysical evaluation of electrical machines.

Mansour Rafiee received his B.Sc. degree from the Sharif University of Technology in 1981, M.Sc. degree from KNT University of Technology in 1996 and Ph.D. Degree from Iran University of Science and Technology (IUST) in 2006, all in electrical engineering. He is currently Associate Professor in Shahid Beheshti University (SBU) and his current research interests include modeling and analysis of renewable energy, power electronics, electrical machines and drives.